Earth and Planetary Science Letters 482 (2018) 171–180

Contents lists available at ScienceDirect

Earth and Planetary Science Letters

www.elsevier.com/locate/epsl

Hot pressing in conduit faults during lava dome extrusion: Insights from Mount St. Helens 2004–2008

Amy G. Ryan [a,*], Elizabeth A. Friedlander [a], James K. Russell [a], Michael J. Heap [b], Lori A. Kennedy [a]

[a] Volcanology and Petrology Laboratory, Department of Earth and Ocean Sciences, University of British Columbia, 2020-2207 Main Mall, Vancouver, BC, V6T 1Z4, Canada

[b] Géophysique Expérimentale, Institut de Physique de Globe de Strasbourg (UMR 7516 CNRS, Université de Strasbourg/EOST), 5 rue René Descartes, 67084 Strasbourg cedex, France

ARTICLE INFO

Article history:
Received 28 June 2017
Received in revised form 2 November 2017
Accepted 5 November 2017
Available online 16 November 2017
Editor: T.A. Mather

Keywords:
lava-dome
volcanic-fault-gouge
permeability
densification
sintering
hot-pressing

ABSTRACT

Rhyodacitic volcanoes such as Mount St. Helens (MSH), Soufrière Hills, Mount Unzen and Mount Pelée erupt spines mantled by layers of magma-derived cataclasite and fault gouge. MSH produced seven lava spines from 2004–2008 composed of low-porosity, compositionally uniform, crystalline dacite. Dome extrusion was attended by continuous 'drumbeat' seismicity, derived from faulting along the conduit margin at 0.5–1 km depth, and evidenced by the enveloping gouge layers. We describe the properties of the gouge-derived fault rocks, including laboratory measurements of porosity and permeability. The gouge varies from unconsolidated powder to lithified low-porosity low-permeability fault rocks. We reconstruct the subsurface ascent of the MSH magma using published field observations and create a model that reconciles the diverse properties of the gouge with conditions in the conduit during ascent (i.e. velocity, temperature). We show lithification of the gouge to be driven by 'hot pressing' processes, wherein the combination of elevated temperature, confining pressure and dwell-time cause densification and solid-state sintering of the comminuted, crystal-rich (glass-poor) gouge. The degree of gouge lithification corresponds with residence time in the conduit such that well-lithified materials reflect extended times in the subsurface due to slower ascent rates. With this insight, we suggest that gouge competence can be used as a first-order estimate of lava ascent rates. Furthermore we posit gouge lithification, which reduces porosity and permeability, inhibits volcanic outgassing thereby increasing the potential for explosive events at spine-producing volcanoes.

1. Introduction

The wide range of eruption styles and resulting landforms associated with the effusive eruption of rhyodacitic magma are an expression of magma rheology and eruptive flux. This is particularly true for the diverse array of morphologies presented by lava domes (Fink and Griffiths, 1998; Sparks et al., 2000; Watts et al., 2002; Cashman et al., 2008; Heap et al., 2016). An end-member of rhyodacitic lava domes that has received much attention in recent years are the spectacular lava spines observed at Mount Unzen, Japan (1990–1995; Nakada and Motomura, 1999; Nakada et al., 1999), Soufrière Hills volcano, Montserrat (1995–2003 and 2005–2013; Watts et al., 2002), and Mount St. Helens (MSH), Washington, USA (2004–2008; Iverson et al., 2006; Cashman et al., 2008).

These spines of lava share a number of features. First, the rocks that form the spines are highly crystallized, typically featuring high phenocryst contents and a microlitic groundmass (Nakada and Motomura, 1999; Sparks et al., 2000; Pallister et al., 2008; Cashman et al., 2008; Cordonnier et al., 2009). Groundmass glass (quenched rhyolitic melt) is subordinate (<15 vol%) and can be as low as <2 vol% (Sparks et al., 2000; Watts et al., 2002; Smith et al., 2011). Second, the spine-forming lava is typically dense – fractional porosities of extruded spine lavas are often measured to be less than 0.1 (Cashman et al., 2008; Cordonnier et al., 2009; Kennedy et al., 2009; Gaunt et al., 2014; Heap et al., 2016). Third, lava spines erupt at low extrusion rates (0.25–2 $m^3\,s^{-1}$; Nakada et al., 1999; Watts et al., 2002; Cashman et al., 2008; Holland et al., 2011) leading to low eruption temperatures and high degrees of crystallinity (i.e. low melt fraction) and, thus, high bulk viscosities (10^9 to 10^{14} Pa s; Nakada and Motomura, 1999; Sparks et al., 2000; Cordonnier et al., 2009; Holland et al., 2011). Indeed, instances of spine formation are restricted to high vis-

* Corresponding author.
E-mail address: aryan@eoas.ubc.ca (A.G. Ryan).

https://doi.org/10.1016/j.epsl.2017.11.010
0012-821X/

Table 1
Surface observations of the 2004–2008 eruption at Mount St. Helens, including: date range for each event, onset day (t), duration (Δt; days), volumetric (Q; $m^3\,s^{-1}$) and linear (U; $m\,d^{-1}$) extrusion rates and spine volume (V; $\times 10^6$ m^3) (Vallance et al., 2008; Schilling et al., 2008). We include calculated spine volumes (V_i; $\times 10^6$ m^3) and lengths (L_i; m), and the width of the fault zones occupied by gouge-derived material (w; m), measured in August 2010.

Event	Date[a]	t	Δt	Q	U	V[d]	V_i[e]	L_i[e]	w
Pre-seismicity	Sep 23–30 2004	0	8	–	–	–	–	–	–
Vent clearing	Oct 1–10 2004	8	10	7–12	>10	10	8.2 ± 2.2	261	–
Spine 1	Oct 11–15 2004	18	5	2–3	15–20	2	1.1 ± 0.2	34	–
Spine 2	Oct 15–24 2004	23	9	3	25	4	2.3	74	–
Spine 3	Oct 25–Dec 18 2004	32	55	4–6	8–11	21	23.8 ± 4.7	756	–
Spine 4	Dec 19 2004–Apr 9 2005	87	112	1.5–2.5	5–8	18	19.4 ± 4.8	616	0.2–2.6
Spine 5	Apr 10–Jul 31 2005	199	113	1–1.5	3–6	15	12.2 ± 2.4	388	1–1.5
Spine 6	Aug 1–Oct 9 2005	312	70	1.5–2	3–4	8	10.6 ± 1.5	337	–
Spine 7	Oct 10 2005–Jul 31 2007[b]	382	660	0.5–1	0.5–2[c]	25[d]	42.8 ± 14.3	1361	0.03–0.6
Endogenous growth	Aug 1 2007–Jan 27 2008[c]	1042	180	–	–				–
Total						93 ± 4[d]	112 ± 28	3829	

[a] Transition periods included in duration of the following spine.
[b] Approximate date for the end of spine 7 extrusion inferred from 2004–2008 time lapse videos for dome growth and crater glacier advance (https://volcanoes.usgs.gov/volcanoes/st_helens/multimedia_videos.html).
[c] End date for eruption, and minimum extrusion rate for spine 7 from the Global Volcanism Program bulletins.
[d] Total volume from Mastin et al. (2009); volume of spine 7 by subtraction.
[e] $V_i = (Q_i \Delta t_i)$; $L_i = (Q_i \Delta t_i)/(\pi(100)^2)$ where 100 m is the radius of the conduit (Iverson et al., 2006).

cosity magmas (andesite to dacite). Lastly, and most pertinent to this study, extruded lava spines, including those erupted at MSH, Soufrière Hills volcano, Mount Unzen, Mount Usu (Japan) and Mount Pelée (Martinique), commonly feature smooth or striated surfaces (Minakami et al., 1951; Fink and Griffiths, 1998; Sparks et al., 2000; Iverson et al., 2006; Cashman et al., 2008; Pallister et al., 2013) comprising a cm to m thick carapace of finely comminuted magma.

The carapace material is fault gouge formed by brittle deformation at the conduit–wall rock interface, where shear stresses are greatest (Sparks et al., 2000; Cashman et al., 2008; Kennedy et al., 2009; Kendrick et al., 2012; Hornby et al., 2015). Small, rapid slip events at this interface create a cylindrical fault zone along the outer margins of the highly viscous, rising magma, and convert the crystallized lava into a fine-grained fault gouge (e.g., Nakada and Motomura, 1999; Watts et al., 2002; Iverson et al., 2006; Neuberg et al., 2006; Pallister et al., 2008; Cashman et al., 2008; Kennedy et al., 2009; Kennedy and Russell, 2012; Gaunt et al., 2014; Kendrick et al., 2014; Hornby et al., 2015; Lamb et al., 2015). Evidence for these slip events is provided by the shallow (depths of 1 to 0.5 km) 'drumbeat' seismicity frequently recorded during spine-forming eruptions (Iverson et al., 2006; Moran et al., 2008a; Umakoshi et al., 2008; Pallister et al., 2013; Lamb et al., 2015; Hornby et al., 2015). Of interest, the extruded fault gouge material is extremely variable in physical and textural properties, ranging from unconsolidated powder to dense lithified fault rock (Minakami et al., 1951; Cashman et al., 2008; Kendrick et al., 2012; Pallister et al., 2013; Hornby et al., 2015).

Our question is: how does the conduit fault gouge lithify so effectively within the short timescales the shallow depths of origin imply? The process operates rapidly on essentially crystalline material (i.e. little to no glass/melt) even at moderate volcanic temperatures (<750 °C; Vallance et al., 2008). The MSH 2004–2008 spine-forming eruptions offer a singular opportunity to address this question because of the extensive array of associated geological observations and geophysical data. We use new laboratory measurements of porosity and permeability on samples of gouge rocks from three different spines at MSH to quantify the extent of lithification. We then use the observations from the MSH eruptions to reconstruct the ascent and thermal history of the individual magma packets that fed each of the seven lava spines. The reconstructions constrain the time–temperature–pressure window for the transformation processes that convert the fault gouge into competent, low-porosity and low-permeability fault rocks (i.e. lithification). Our analysis suggests that hot pressing, similar to that used commercially to produce ceramics and semi-conductors, drives lithification of the volcanic fault gouge associated with lava spine-producing volcanoes. This result is notable because it indicates there is an undiscovered lithification mechanism operating within the upper conduit during spine-producing eruptions that, significantly, does not require the presence of melt or the precipitation of new mineral phases.

2. A case study: Properties of MSH gouge

From 2004 to 2008 MSH produced seven discrete lava spines, each comprising a core of low-porosity dacite enveloped by a carapace of variably indurated fault gouge (Iverson et al., 2006; Cashman et al., 2008; Kennedy et al., 2009; Kendrick et al., 2012, 2014). Prior studies concluded that the magma crystallized and solidified at ~1 km depth (Iverson et al., 2006; Pallister et al., 2008; Cashman et al., 2008) and then was pushed to the surface along cylindrical, conduit wall-parallel, fault zones. Brittle deformation along these faults resulted in the production of fine-grained, comminuted gouge from the solidified, crystal-rich, ascending dacite. Rhythmic seismicity (i.e. 'drumbeat' seismicity) was observed throughout the MSH eruption although the seismic energy released decreased with time (e.g., Iverson et al., 2006; Moran et al., 2008a) perhaps reflecting a decrease in ascent rate as the eruption waned. Previous workers interpreted the microseismic events as stick-slip events localized in the gouge along the conduit wall (Iverson et al., 2006; Cashman et al., 2008; Pallister et al., 2013). In contrast, we suggest the seismicity derives from relatively high stress drop events related dominantly to the production of gouge from the crystallized dacite magma (i.e., Kennedy et al., 2009; Kennedy and Russell, 2012). There were also low levels of magmatic outgassing measured throughout the eruption (Gerlach et al., 2008) focused along the conduit parallel faults (Rowe et al., 2008).

2.1. Textural organization, granulometry and mineralogy

The nature and properties of the enveloping fault gouge are well described in the literature, with a particular focus on the carapaces at spines 4 and 7 (Cashman et al., 2008; Pallister et al., 2008; Kennedy et al., 2009; Kendrick et al., 2012; Gaunt et al., 2014). Table 1 reports our field measurements of the thickness of the fault gouge carapaces. The gouge material encasing spines 4 and 5 is 1 to 3 m thick whereas the gouge is considerably thinner (0.03–0.6 m) at spine 7 (Table 1). The conduit-parallel fault

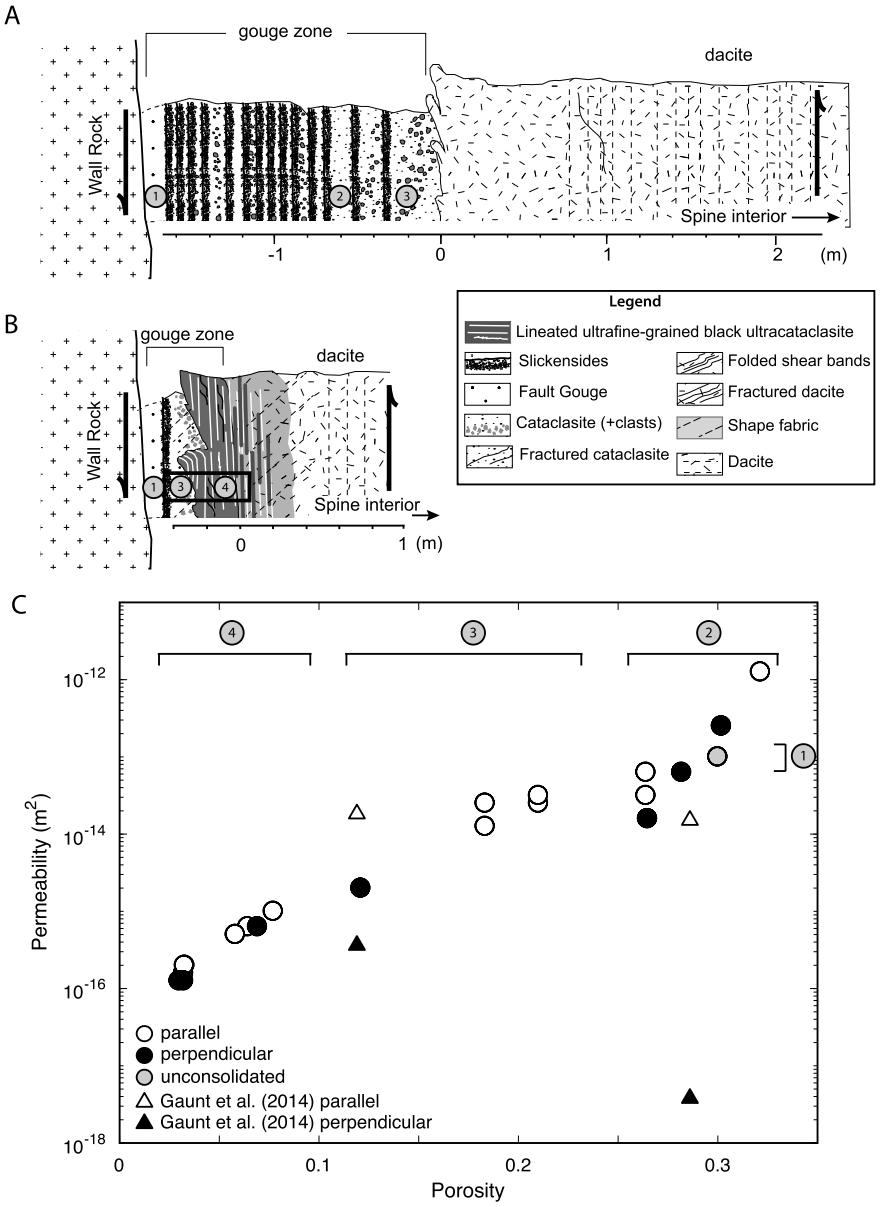

Fig. 1. Diversity of fault zone geometries and properties at MSH. (a) Summary log for the fault zone at spine 4, a partially lithified carapace. Units include unconsolidated gouge, indurated gouge crosscut by slickensides, and cataclasite. Numbered regions show the approximate locations of samples shown in panel (c). (b) Summary log for the fault zone at spine 7, an extensively lithified carapace. The fault zone is thin and the units are gradational from unconsolidated material to highly competent ultracataclasite. The black box outlines the approximate location of sample shown in Fig. 2. (c) Measured porosities and permeabilities for unconsolidated gouge (gray circle), and variably lithified gouge from this study (circles) and Gaunt et al. (2014) (triangles). Sample cores were cut parallel (open symbols) or perpendicular (closed symbols) to planar fabric taken as parallel to extrusion direction. Cores from the ultracataclasite have the lowest measured porosities and permeabilities, while indurated gouge cores have the highest values.

zones show a lithostratigraphic organization that is generalized in Fig. 1a. From the conduit wall to the interior of the spine, the fault zone comprises: (1) ultracataclastic slickensides on the exterior surface, (2) unconsolidated fault gouge hosting thin slickenside layers, (3) indurated gouge, (4) cohesive cataclasite, (5) sheared dacite, and (6) massive dacite (Fig. 1a). Spine 7 is significantly different in that it hosts a foliated ultracataclasite immediately beneath the indurated gouge (Figs. 1b and 2). This ultracataclasite is absent from other spines where less dense cataclasite takes its place (Fig. 1a; Supplementary Information, Fig. S1) (Cashman et al., 2008; Pallister et al., 2013; Gaunt et al., 2014).

The MSH gouge comprises mineral and lithic particles of varying size. Hand sample and thin section observations on materials from multiple spines, and quantitative analysis of the unconsolidated gouge (Supplementary Information, Fig. S2), show grain sizes spanning 1 μm to 10 cm, which accords with previous grain size determinations (e.g., Iverson et al., 2006; Cashman et al., 2008; Kennedy et al., 2009; Kendrick et al., 2012; Kennedy and Russell, 2012; Pallister et al., 2013). All particles, regardless of size, are angular to subrounded. Fig. 2 illustrates the gradual change in grain shape and size across the gouge carapace on spine 7, including the ultracataclasite.

The fault gouge derives from the dacitic magma and is compositionally uniform, reflecting the chemical homogeneity of the erupting magma (~65 wt% SiO_2; Pallister et al., 2008, 2013; Cashman et al., 2008; Thornber et al., 2008; Kendrick et al., 2012). In Table S1 (Supplementary Information) we report the mineralogy of our gouge samples as determined by X-ray diffraction (XRD), which includes plagioclase, amphibole, orthopyroxene, ox-

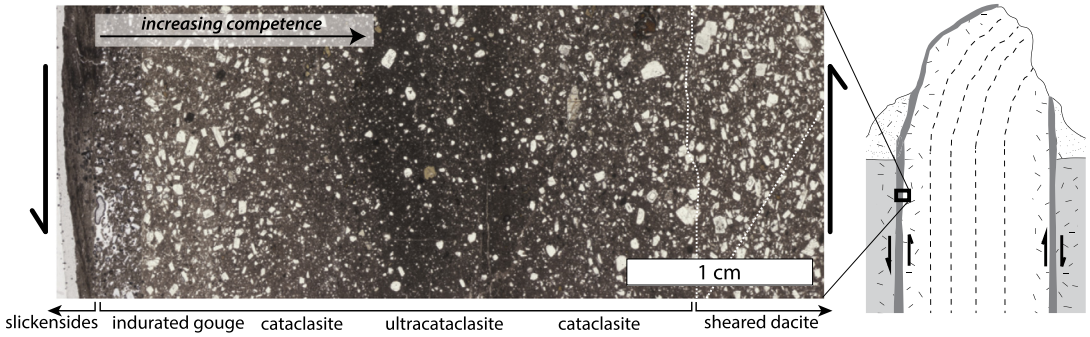

Fig. 2. Grain size, shape and texture of an extensively lithified gouge-rock (spine 7). The composite photomicrograph is oriented as it formed in the conduit (see cartoon) and shows the gradation in competence and texture from spine exterior to the interior. From left to right the material includes: capping ultrafine-grained ultracataclasite layers (*slickensides*); large, angular mineral grains set in a light brown matrix (*indurated gouge*); mineral grains of gradually decreasing size, showing increased grain rounding (*cataclasite*); dark gray/black region having few large and well-rounded mineral grains (*ultracataclasite*); mineral grains of gradually increasing size set within a dark brown matrix (*cataclasite*); numerous angular phenocrysts within a microcrystalline groundmass showing a weak shape fabric (*sheared dacite*).

Table 2
Measured total fractional porosity (ϕ) and steady-state permeability ($\log_{10} k$; m^2) for MSH gouge samples from different spines, cored in different orientations. Replicate measurements are also reported.

Parallel				
Spine	Sample	ϕ[a]	$\log_{10} k$	$\log_{10} k$
4	4_3a(2)_1	0.32	−11.9	
5	5_2b(2)_1	0.26	−13.2	−13.5
7	7_3c_3	0.21	−13.5	−13.6
7	7_3c_1	0.18	−13.6	−13.9
7	7_4b_1	0.08	−15.0	
7	7_4b_3	0.06	−15.2	
7	7_4b_5	0.06	−15.3	−15.3
7	7_5j_1	0.03	−15.7	
7	7_5j_3	0.03	−15.7	
Perpendicular				
Spine	Sample	ϕ[a]	$\log_{10} k$	$\log_{10} k$
4	4_3a(2)_4	0.30	−12.6	−12.6
4	4_3a(2)_2	0.28	−13.2	
5	5_2b(3)_2	0.26	−13.8	−13.8
7	7_3c_4	0.12	−14.7	
7	7_4b_2	0.07	−15.2	
7	7_5j_2	0.03	−15.9	
7	7_5j_4	0.03	−15.9	−15.8
Unconsolidated				
Spine	Sample	ϕ[a]	$\log_{10} k$	$\log_{10} k$
5	5_0_SM	0.30	−13.0	−13.0

[a] Isolated porosity, calculated from the density of powdered gouge and the measured skeletal density of the cores, is 0.01–0.02 for all samples.

ides, quartz, tridymite and cristobalite (cf. Pallister et al., 2008, 2013; Cashman et al., 2008; Kendrick et al., 2012). The abundance of these phases, including silica polymorphs, does not vary between spines or with increasing sample competence. Our analysis of the fault zone materials from spines 4, 5 and 7 indicates a common macroscale textural organization, grain size distribution and composition. However, there are substantial differences in fault zone thicknesses and in the competence of the fault gouge.

2.2. Porosity and permeability

We measured the porosity and permeability of samples of MSH gouge (Table 2) and use these new measurements to quantify the changes in physical properties attending gouge lithification. Previous measurements of porosity and permeability for MSH dome-forming lavas are available (see Heap et al., 2016, and references within) but measurements on the fault zone materials are few (Kendrick et al., 2012; Gaunt et al., 2014). Our measurements are made on the unconsolidated material and on cylindrical samples (25.4 mm in diameter and 26–51 mm in length) cored from blocks of the texturally distinct units within the fault zones at spines 4, 5 and 7. Samples were cored in two orientations that are parallel and perpendicular to planar fabrics. We assume the planar fabrics are oriented parallel to extrusion direction and to the conduit walls. Connected porosity was measured using a helium pycnometer, and permeability was measured using a benchtop helium permeameter (confining pressure of 2.5 MPa) on oven-dry cores using the steady-state flow method (see Heap et al., 2016, for a full description of the steady-state method) (Table 2).

Values of permeability plotted as a function of total porosity (Fig. 1c) show porosity and permeability to vary across the sample suite by one and four orders of magnitude, respectively. These two physical properties are strongly correlated with the apparent competence of the fault gouge material (Fig. 1c). The gouge rocks furthest from the conduit boundary have low porosities and permeabilities (0.03 and $\sim 10^{-16}$ m^2; Fig. 1; Table 2), whereas porosity and permeability are greatest at the wall–rock interface (0.32 and $\sim 10^{-12}$ m^2; Fig. 1; Table 2). Gaunt et al. (2014) also measured an elevated porosity at the wall–rock interface. Our data show no measurable anisotropy in permeability in the low-porosity samples cored parallel and perpendicular to the direction of extrusion. In contrast, we observe anisotropy in the permeability of higher porosity gouge samples (i.e. those closer to the wall–rock interface) up to 1 order of magnitude (Fig. 1; Table 2). The data of Gaunt et al. (2014) show an even larger anisotropy of permeability (4 orders of magnitude) in their high-porosity samples of gouge. Differences between data from these two studies attest to the heterogeneous nature of the fault zone materials.

3. Magma ascent in the conduit

The 2004–2008 eruption of MSH lasted 42 months, during which time seven spines were extruded sequentially from the same vent. Drumbeat seismicity occurred for the duration of the eruption and is interpreted to result from repetitive stick-slip or fracture-slip faulting localized at the conduit margin (e.g., Iverson et al., 2006; Moran et al., 2008a; Kendrick et al., 2012; Kennedy and Russell, 2012; Pallister et al., 2013), resulting in the formation of fault gouge. While the decrease in the rate and magnitude of these events over time (e.g., Moran et al., 2008a) may signal the waning of the eruption (Scott et al., 2008), the persistent microseismicity suggests the continued production of crystal-rich (glass-poor), unconsolidated fault gouge at depth. At the surface, the gouge layer is variably densified: spines 4 and 5 have carapaces of loose powder, indurated gouge, and relatively porous cataclasite (Figs. 1 and S1). In contrast, the carapace enveloping spine 7 is composed of unconsolidated gouge that grades to a highly com-

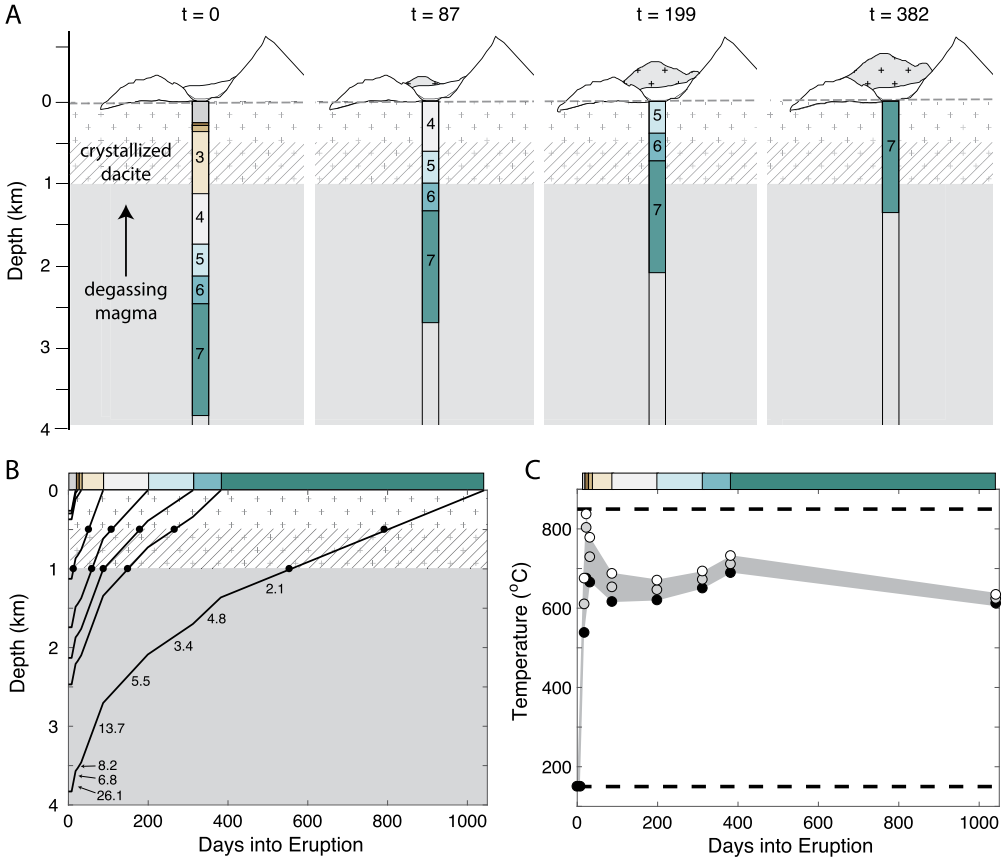

Fig. 3. "Top-down" model for spine extrusion. (a) Schematic cross sections of MSH showing the position of dacite spines at $t = 0$ (onset of seismicity), 87, 199 and 382 days (the start of spine 4, 5 and 7 extrusion, respectively). The length of each spine (L_i) is given in Table 1. The field of crosses (+) above 1 km and the crosshatched region (1 to 0.5 km) denote the depth where the dacite is solidified, and the zone where gouge formation occurs, respectively (Cashman et al., 2008). (b) Modeled ascent paths for each spine. Colors and patterned fields as in panel (a). Ascent paths for the top and bottom of the parcel of solidified magma that makes up each spine (color bar) have been reconstructed in depth-time space. The ascent rate of a spine is not constant; the slopes (values on right side) are calculated by dividing L_i by Δt_i. Black dots show when the top (or bottom) of each spine reaches 1 and 0.5 km depth. As ascent rates decrease during the eruption (shallowing slope of ascent path curves), the later spines (and gouge) have longer residence times. (c) Results of thermal model predicting the temperature of gouge as a function of time. Colors as in panel (a). Dashed lines are boundary condition temperatures: wall rock = 150 °C, ascending magma = 850 °C (see text). The modeled temperatures at the contact with the wall rock, and 0.5 and 1 m in to the conduit are shown as closed, gray, and open circles respectively (Table 3).

petent, dense, low-permeability ultracataclasite (Figs. 1 and 2). The variable competence of the fault zone rocks enveloping these spines indicates that (1) the gouge is progressively lithified during transit to the surface, and (2) the conditions associated with the formation of the ultracataclasite at spine 7 are in some way different from the lithification conditions for the less competent gouge-derived material at spines 4 and 5.

Observations collected for each spine eruption include: surface-resolved linear extrusion rates (U; $\mathrm{m\,s^{-1}}$), volumetric extrusion rates (Q; $\mathrm{m^3\,s^{-1}}$), eruption durations (Δt; days) and approximate erupted volumes (V; $\mathrm{m^3}$) (Table 1; Vallance et al., 2008; Schilling et al., 2008). The linear and volumetric extrusion rates decay logarithmically with time such that rates for spine 7 are an order of magnitude lower than for spine 1 (Table 1).

We use these observational data to reconstruct the pre-2004 eruption magma column (Fig. 3a) and to model the ascent of the individual (i^{th}) parcels of magma that fed each spine (Fig. 3b; Table 3). We adopt a cylindrical geometry for the magma-filled conduit (as suggested by Pallister et al., 2008, 2013), where the diameter (D) is approximated to 200 m (e.g., Iverson et al., 2006). Using this idealized geometry, the median observed volumetric extrusion rate (Q_i) and eruption duration (Δt_i), we calculate the length (L_i; m) of each cylindrical parcel of lava (Table 1). The total length of the subsurface magma column at the start of the eruption is the sum of these modeled values, which we estimate as 3.8 km (Table 1). This approach allows us to model the position of the discrete parcels of magma within a vertical column at the start of the eruption ($t = 0$) and throughout the eruption. Fig. 3 illustrates the progressive ascent (i.e. position in the conduit) of these magma parcels as a function of time including the time at which each portion of magma reaches depths of 1, 0.5, and 0 km (Fig. 3b; Table 3).

The slopes of depth-time paths define ascent rates for the individual spine-forming magma packets as a function of depth. These slopes, plotted as lines in Fig. 3b, show that the magma ascent rate was not constant but decreases with time throughout the 2004–2008 eruption of MSH (values in Fig. 3b). It is also clear that the ascent rates of individual packets of magma become more complex as the eruption progresses. Note that the modeled ascent rates differ from the values reported for spine extrusion rates because the observed linear extrusion rates (i.e. U) only correspond to magma ascent rate at the very top of the conduit. For example, later parcels of magma are moving faster in the subsurface than the extrusion rates observed at the surface would suggest. We report the maximum and minimum calculated ascent rates (v) at depths <1 km in Table 3.

Shear strain rates associated with syn-eruptive deformation of the conduit margin materials during faulting are calculated from these reconstructed ascent rates at depths <1 km (v, Table 3). Shear strain rates (γ') within the fault zone core are calculated as v/w where w is the thickness of the unit over which strain is distributed (i.e. the thickness of fault zone core; Table 1). Val-

Table 3
Modeled parameters for the 2004–2008 MSH lava spine eruption, including: the eruption day (t_x) when the top of each spine reached the surface (0 km), 0.5 km and 1 km; the residence time over those depth intervals (Δt_{x-x}; d); ascent rates at <1 km depth (v; m d^{-1}); and calculated shear strain rates (γ'; s^{-1}). Also included are the Peclet number (Pe; see text) and model temperatures (°C; at 1 km depth) at the conduit–wall rock interface (0 m), as well as 0.5 m and 1 m in to the conduit.

Event	Transit day			Ascent rate		Shear strain rate[a]		Peclet number		Temperature			Residence time	
	t_0	$t_{0.5}$	t_1	v_{min}	v_{max}	γ'_{min}	γ'_{max}	Pe_{min}	Pe_{max}	0 m	0.5 m	1 m	$\Delta t_{0.5-0}$	$\Delta t_{1-0.5}$
Vent clearing	8	–	–	26.1	26.1	–	–	$10^{4.8}$	$10^{4.8}$	150	–	–	–	–
Spine 1	18	–	–	6.8	26.1	–	–	$10^{4.2}$	$10^{4.8}$	538	610	675	–	–
Spine 2	23	–	–	6.8	26.1	–	–	$10^{4.2}$	$10^{4.8}$	675	803	837	–	–
Spine 3	32	–	–	6.8	26.1	–	–	$10^{4.2}$	$10^{4.8}$	665	729	778	–	–
Spine 4	87	51	13	13.7	26.1	6.1×10^{-5}	1.5×10^{-3}	$10^{4.5}$	$10^{4.8}$	616	653	687	36	38
Spine 5	199	108	59	5.5	13.7	4.2×10^{-5}	1.6×10^{-4}	$10^{4.1}$	$10^{4.5}$	620	646	670	91	49
Spine 6	312	179	88	5.5	5.5	–	–	$10^{4.1}$	$10^{4.1}$	650	672	693	133	91
Spine 7	382	266	149	3.4	5.5	6.7×10^{-4}	2.1×10^{-3}	$10^{3.9}$	$10^{4.1}$	689	711	732	116	117
Base of spine 7	1042	792	554	2.1	2.1	–	–	$10^{3.7}$	$10^{3.7}$	612	624	634	250	238

[a] $\gamma'_{min} = v_{min}/w_{max}$; $\gamma'_{max} = v_{max}/w_{min}$ (Table 1).

ues for γ' vary from 4.3×10^{-5} to 2.1×10^{-3} s^{-1} (Table 3). The fault zones at spines 4 and 5 are significantly wider than those in spine 7 (1–3 m *vs.* 0.03–0.6 m) and, therefore, values of γ' are similar, despite the differences in ascent velocities (Table 3). Variations in shear strain rate are therefore unlikely to explain the differences in physical and textural properties and densification of the fault gouge mantling the different spines.

The reconstructed ascent rates are also used to constrain the temperatures in the rising packets of magma for each spine (Table 3). The model is adapted from Jaluria and Torrance (1986) and Russell (1988) and accounts for conductive heat transfer to the conduit walls *vs.* advective transport within the magma as it ascends the conduit from a depth of ~1 km. The modeling establishes the temperature distributions at three points – at the conduit–wall rock interface, and 0.5 and 1 m into the conduit from the interface. The thermal model uses an initial temperature of 850 °C for the dacite magma, which is just below the peak temperature estimated for crystallization at ~1 km (857 to 936 °C; Blundy et al., 2008; Pallister et al., 2008). The Peclet number (Pe) is calculated as $v \times D/\alpha$, where α is the thermal diffusivity (taken as 10^{-6} m^2 s^{-1}). Even for the slowest ascent rates of the MSH dacite (e.g., 2.1 m d^{-1}) the computed Pe values are much greater than unity ($10^{3.7}$; Table 3), indicating that advective transport of heat dominates over conductive heat loss to the wall rocks during ascent (Russell, 1988).

At the start of the eruption, the ascent rates in the conduit are high (Table 3), heat transfer is dominantly advective (little conductive heat loss), and magma temperatures are kept high (Fig. 3c). As the eruption proceeds and ascent rates decrease there is a greater capacity for conductive heat loss (e.g., spine 7; Table 3), although this is mitigated somewhat by the fact that the wall rocks have already been heated by the passage of previous magma (i.e. spines 1–6) (Fig. 3c; Table 3). The temperatures of wall rocks at the conduit interface increase rapidly in the first three weeks of the eruption and remain between 620 and 690 °C for the remainder of the eruption (Fig. 3c; Table 3). Model temperatures for gouge 0.5 m and 1 m from the conduit–wall rock interface follow the same heating trend where temperatures peak during the ascent of spine 2 (803 and 837 °C, respectively) and then stabilize at 630 and 730 °C for the rest of the eruption (Fig. 3c; Table 3). Our model values for the fault zone temperature are similar to those measured at the surface by thermal imaging of cracks in the carapace (Vallance et al., 2008). The results provide a range of temperatures at which gouge lithification must operate. However, these calculations show that variations in temperature during ascent are insufficient to account for the variable lithification of fault gouge mantling the different spines.

4. Hot pressing: A model for lithification of volcanic gouge

The slow ascent of highly crystalline rhyodacite magma in volcanic conduits supports both viscous and brittle deformation (e.g., Lavallée et al., 2007; Cordonnier et al., 2009; Smith et al., 2011; Okumura et al., 2016). Brittle deformation is commonly restricted to the conduit walls and manifest as a conduit-parallel fault zone composed of fault gouge derived from comminuted, holocrystalline magma (e.g., Goto, 1999; Neuberg et al., 2006; Holland et al., 2011; Kendrick et al., 2014). At MSH, the gouge is produced at relatively shallow depths (~0.5 to 1 km; e.g., Cashman et al., 2008) corresponding to low lithostatic pressures (~12.5 to 25 MPa). Magma temperatures in the conduit are relatively low (630–730 °C; Table 3; Vallance et al., 2008) and residence times within the volcanic conduit are generally short (months to <2 yr). The resulting domes and spines are extruded with carapaces of fault gouge that are extremely variable in terms of their physical properties (e.g., porosity, permeability), varying from unconsolidated, low-cohesion powder to dense, low-permeability, fault rocks. These facts posit two questions: firstly, and empirically, what controls the degree of lithification of the volcanic fault gouge? Secondly, and more fundamentally, what is the process that drives lithification within the narrow time–temperature–pressure window?

Our analysis of the MSH eruptions has shown that the most lithified gouge is associated with spine 7 (i.e. the low-porosity, low-permeability ultracataclasite). Previous work on spine 7 by Kendrick et al. (2012) distinguished four structurally distinct layers within the spine 7 fault zone: (1) an outer surface of indurated gouge (L1) that crosscuts (2) a dark, banded layer (L2; i.e. the ultracataclasite in Figs. 1b and 2) which, itself, grades into (3) a moderately sheared layer (L3), and (4) the undeformed dacite core (L4). These authors suggested that the L2 layer contained evidence of frictional melting within the gouge caused by seismogenic slip events that produced a pseudotachylite (e.g., Lavallée et al., 2012; Kendrick et al., 2012, 2014). Although localized frictional melting may be present, this mechanism cannot explain the pervasive, variable densification and lithification of the fault gouge that envelops each spine (Fig. 1c). Variably indurated fault gouge is found on all spines at MSH, although spine 7 is noteworthy for the high degree of competence of the gouge-derived ultracataclasite. We also reiterate that the comminuted solidified magma is essentially devoid of glass, thus precluding lithification by viscous sintering (as is the case for glassy materials; see Quane et al., 2009; Vasseur et al., 2013; Wadsworth et al., 2017). There is also no textural evidence nor modal mineralogical variations (Supplementary Information, Table S1) suggesting the gouge was lithified by cementation processes involving fluids. Though outgassing magmatic volatiles passed primarily through the gouge-filled fault zone (Rowe et al., 2008), the low initial volatile content of this MSH

magma (e.g. Pallister et al., 2008; Scott et al., 2008; Gerlach et al., 2008) precludes cementation as a significant lithification mechanism.

The variations in the reconstructed ascent rates for each spine-forming magma translate into substantial differences in subsurface residence times (Table 3). The ascent paths (depth-time; Fig. 3b) define the total residence times for each packet of magma and its associated fault gouge at depths <1 km (i.e. $\Delta t_{1-0.5}$, $\Delta t_{0.5-0}$; Table 3). The total subsurface residence time for each magma packet increases as the eruption progresses from 74 to 448 days (Table 3). The last material erupted (spine 7 extrusion) has the longest residence time. Therefore, the unconsolidated gouge associated with spine 7 would have remained at elevated pressure and temperature for ~150–400 days longer than the gouge mantling spine 4, and ~100–350 days longer than the gouge mantling spine 5. We suggest that, to a first order, the degree of lithification of fault gouge reflects the total time (residence time) spent at elevated temperature and at lithostatic pressure (i.e. depth). Based on the empirical evidence, it appears that slower ascent rates provide the longer residence times at the elevated temperature and pressure conditions required for lithification of the fault gouge.

Hot pressing (HP) and hot isostatic pressing (HIP) are two manufacturing processes used to densify granular material by subjecting the particles to high temperatures under differential (HP) or hydrostatic (HIP) pressure (Ramqvist, 1966; Rahaman, 2003). These methods are used extensively in metallurgy and the production of ceramics. They are also common practice for fabricating synthetic samples for rock deformation experiments (e.g., Rybacki et al., 2003; Kushnir et al., 2015) or studying densification by viscous sintering (i.e. welding) in volcanic systems (e.g., Quane et al., 2009; Heap et al., 2014). They are effective in densifying materials where the elevated temperature–pressure conditions activate specific sintering processes. In the case of crystalline materials, sintering occurs in the solid-state by diffusion. We contend that the dominant process for lithification of fault gouge materials derived from comminution of solidified magma is 'volcanic hot pressing'. The hot pressing of the crystalline granular material promotes solid-state diffusional processes that bind particles together.

Experimental studies of hot pressing and sintering have explored the effects of temperature, pressure, grain size and time on sintering efficiency in crystalline materials (e.g., White, 1965; Ramqvist, 1966; Rahman, 2003). Rates of densification greatly increase with increasing temperature owing to faster rates of atomic diffusion. Higher pressures can increase the stress on grain boundaries thereby accelerating grain boundary or lattice diffusion and densification rates. Increased time at these conditions leads to greater porosity reduction and increased competence and lithification. Reduced grain sizes support higher densification rates because diffusion is facilitated by the increase in surface area to volume ratios, and the reduced distances to and between grain boundaries.

To better constrain the grain radius of particles responsible for the gouge densification process at MSH, we use the Wadsworth et al. (2016) permeability model, which is applicable to densifying granular materials. This universal scaling model illustrates the influence of particle radius on densification dynamics regardless of the densifying mechanism. Specifically, it models the relationship between permeability and adjusted or 'scaled' porosity (i.e. total porosity minus 0.03; see Wadsworth et al., 2016, for justification) as a function of grain size. We have plotted our permeability and porosity (adjusted) data (Fig. 1c; Table 2) on a diagram contoured for grain size using the Wadsworth et al. (2016) model (Fig. 4a). Our data, comprising a suite of materials from unconsolidated powders to dense rock, cluster along the 10 μm contour (Fig. 4a).

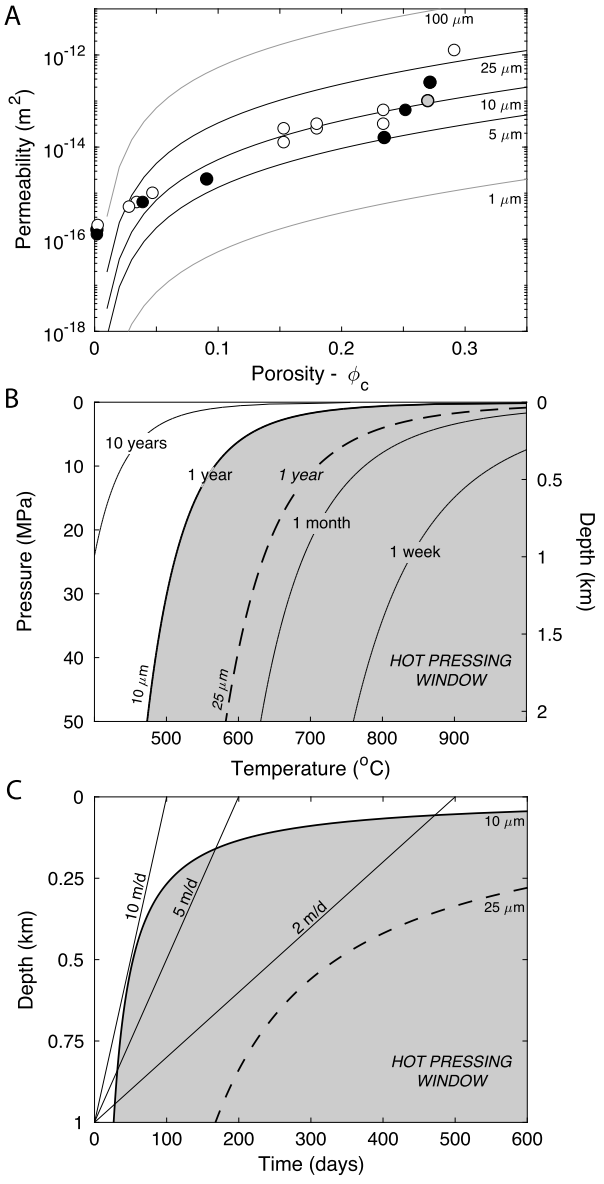

Fig. 4. Hot pressing in volcanic conduits. (a) Our porosity–permeability data (from Fig. 1c) and the universal scaling model from Wadsworth et al. (2016). Contours show the predicted porosity–permeability relationship for particles of a specified grain radius densifying by any mechanism. Data fall along the 10 μm contour, but deviate toward the 100 μm contour at low porosities. From this, we infer that densification of gouge occurs primarily by sintering of small particles. (b) Modeled *minimum* densification time ($t_{\Delta\rho}$; contours) at a given pressure (P) and temperature (T) (Eq. (1)). The prescribed relative density (ρ/ρ_i) is equivalent to transforming an unconsolidated powder (initial porosity ~0.33) to a dense solid (final porosity ~0.0) ($\rho/\rho_i = 1.5$). Grain radius (G) is 10 μm in order to constrain the magnitude of $t_{\Delta\rho}$. Where $t_{\Delta\rho} < 1$ yr, we define a 'hot pressing window' (shaded region) where gouge will be extensively lithified on a short timescale. Where $t_{\Delta\rho} > 1$ yr densification is still occurring, but at a diminished rate so that gouge properties do not change substantially on a timescale similar to that of a spine-producing eruption (white region). An increase in G to 25 μm shifts contours to the right (dashed curve). (c) Influence of ascent rate on the potential for extensive lithification of gouge. Solid curve and shaded region define the 'hot pressing window', where the residence time at depth is greater than $t_{\Delta\rho}$ ($T = 700\,°C$, $\rho/\rho_i = 1.5$, $G = 10$ μm). An increase in G to 25 μm (dashed curve) shifts the 'hot pressing window' to longer times. When the ascent rate of solidified lava (and gouge carapace) is high (10 m d^{-1}, steep line), it moves rapidly from a deeper regions in the conduit where $t_{\Delta\rho}$ is small to shallow regions where $t_{\Delta\rho}$ is large (shown by solid curve). Because residence time is less than $t_{\Delta\rho}$ the ascent path of the lava bypasses the 'hot pressing window' and the gouge will be weakly consolidated when it reaches the surface. Conversely, when ascent rate is slow (2 m s^{-1}, shallow line), gouge resides for an extended time at high P, where $t_{\Delta\rho}$ is small. At these conditions, residence time is greater than $t_{\Delta\rho}$ so densification proceeds quickly and the gouge will be a high competence material when it reaches the surface.

The distribution of our data suggests that the sintering process is facilitated by, or depends on, the smallest particles within the bulk fault gouge material. This inference is supported by experimental and theoretical studies of sintering, which show increased densification rates where particles are small (e.g., Rahaman, 2003; Vasseur et al., 2013; Wadsworth et al., 2017). Furthermore, microstructural observations show that the well-lithified gouge (i.e. cataclasite and ultracataclasite), although poorly sorted, has a high abundance of small particles (Fig. 2; Cashman et al., 2008; Kennedy et al., 2009; Kendrick et al., 2012; Pallister et al., 2013). The implication is that although the gouge comprises a wide range of grain sizes (1 μm to 10 cm; Cashman et al., 2008; Kendrick et al., 2012; Pallister et al., 2013), the larger particles are not active in the lithification process. These passive particles are instead bound together by the progressive sintering and densification of the finer grained matrix. Larger grains (radii up to 100 μm) may only become involved in sintering once the population of smallest grain sizes has been sufficiently reduced. This is shown in Fig. 4a where data for the densest material deviate from the 10 μm contour. At this point, the change in the grain size of the particles may increase the densification time such that sample density would not change appreciably on the timescale of the eruption.

Several authors have developed models for the rate of densification as a function of the parameters discussed above (see references within Ramqvist, 1966). We use the following generalized model from Rahaman (2003) to illustrate schematically the relative influences of pressure (P) and temperature (T) on the *minimum* time necessary to densify ($t_{\Delta\rho}$) a material of a specified grain radius (G) by a fixed amount, dictated by the prescribed relative density (ρ/ρ_i) (Fig. 4b):

$$t_{\Delta\rho} = \left(\ln\frac{\rho}{\rho_i}\right)\frac{G^m kT}{HD\delta P}. \quad (1)$$

In Eq. (1) k is the Boltzmann constant, H is a constant, D is the diffusion coefficient of the rate-controlling species, δ is a shape parameter, and m has a value that depends on the sintering mechanism (e.g., boundary or lattice diffusion) (Rahaman, 2003). In Fig. 4b we show the relationships between temperature, pressure, grain size and minimum densification time, where the modeled change in density is equivalent to converting an unconsolidated power to a dense solid. At elevated pressures (>30 MPa, ~1.25 km), temperature is the dominant control on densification time, as the steep-sloping contours in Fig. 4b show. However, at pressures below 10 MPa (~0.5 km), the contours in Fig. 4b begin to flatten and become more closely spaced: densification rates remain temperature-dependent but the minimum time required for densification increases substantially compared to rates at higher pressures. An increase in the radius of the densifying particles shifts the contours to the right (more time is necessary to densify the material) but does not affect the overall shape of the contours (dashed gray curve, Fig. 4b). Finally, we define a 'hot pressing window' (shaded region, Fig. 4b) where the minimum densification time is less than 1 yr.

Sintering efficiency depends on pressure, temperature and time, which supports our assertion that the degree of lithification reflects residence times in the conduit, and indirectly informs on ascent rate. This relationship is illustrated in Fig. 4c where potential ascent paths, defined by average ascent rate, are compared to the time–pressure window for hot pressing at elevated temperatures. Where the gouge material ascends slowly (2 m d^{-1}, shallow line in Fig. 4c), it remains for an extended time in a high-pressure region of the conduit, where densification rates are high (i.e. Eq. (1)). On this path, material becomes fully lithified because the residence time exceeds the requisite time for densification of this material at conduit temperatures: the result is extrusion of a highly competent, lithified rock (e.g., ultracataclasite; Fig. 2). Conversely, higher ascent rates create paths that completely miss (10 m d^{-1}, Fig. 4c) or only briefly transect (5 m d^{-1}, Fig. 4c) the 'hot pressing window' and are subject to lower rates of densification. The shorter residence times at depth (i.e. higher ascent rates) and the lower rates of densification preclude complete lithification: the gouge will be extruded unconsolidated or only weakly lithified.

5. Implications for eruption dynamics and monitoring

The morphology and stability of lava domes have been shown to correlate with subsurface ascent rates (e.g., Fink and Griffiths, 1998; Watts et al., 2002; Heap et al., 2016). These rates, which differ from extrusion rates observed at the surface, can constrain the rheologic behavior of the magma in the conduit, and can signal the waxing or waning of an eruption. The competence of gouge reflects subsurface residence times, suggesting that the properties of fault gouge mantling lava spines could serve as a geospeedometer, informing on conduit ascent rates. For example, where the carapace comprises unconsolidated or partially indurated gouge, one can forensically infer a relatively rapid subsurface ascent rate. Conversely a well-lithified gouge carapace implies substantially slower ascent rates.

Mount Unzen offers another example. The remnant spines from the 1991–1995 eruption are mantled in gouge layers described as 'sintered', 'welded', and/or 'agglutinated' (e.g. Hornby et al., 2015). A photo of the relict of the 1994–1995 spine and its marginal shear zone (Fig. 2a; Hornby et al., 2015) shows well-lithified gouge, implying slow subsurface ascent. This observation accords well with the low observed extrusion rates (0.25–0.5 m^3 s^{-1}; Nakada et al., 1999), although, as we have shown, observed extrusion rates are not the same as subsurface ascent rates. The spines produced during the 1995–1999 eruption of Soufrière Hills volcano have a different character: the gouge that envelops these spines is poorly-lithified. For example, Watts et al. (2002) describe a smooth-topped lava dome being extruded on October 1, 1996 at a flux of 1.8 m^3 s^{-1} (faster than median extrusion rate of spine 4 at MSH; Table 1). By October 10 portions of the carapace failed, exposing a thick layer of weakly indurated gouge and breccia (Fig. 15a; Watts et al., 2002), reflecting the relatively high observed extrusion rate.

Many active dome- or spine-producing volcanoes are remotely monitored using aerial and terrestrial photography/photogrammetry (e.g., Watts et al., 2002; Schilling et al., 2008; Ryan et al., 2010; Diefenbach et al., 2012), thermal imaging/photogrammetry (e.g., Bernstein et al., 2013; Thiele et al., 2017), and webcams (e.g., Poland et al., 2008; Bull et al., 2013). Remote sensing may provide a means to qualitatively assess the competence of the enveloping gouge layer from the material's angle of repose or from the frequency of sloughing or slumping events. Given the relationship between subsurface ascent rate and properties of the fault gouge, degree of gouge lithification may then be used to infer the acceleration or deceleration of magma in the conduit. Changes in gouge properties, coupled with other observational data, could indicate whether an eruption is waxing or waning.

Marginal fault zones filled with fault gouge and cataclasites are expected to be high-porosity, high-permeability regions supporting efficient passive degassing. The presence of permeable fault zones should therefore inhibit build-up of gas overpressures and preclude the explosive release of trapped gases. However at dome- and spine-producing systems like MSH, gas-charged explosive outgassing events still occur and are localized in the fault zones at the conduit wall (e.g., Rowe et al., 2008; Cashman et al., 2008; Moran et al., 2008b; Holland et al., 2011; Lavallée et al., 2013; Pallister et al., 2013; Gaunt et al., 2014). Changes in fault properties causing a reduction in permeability (e.g., cementation or welding) have been invoked as triggers for explosive events (e.g., Quane et al., 2009; Holland et al., 2011). Hot pressing represents

another means of causing a permeability reduction leading to re-pressurization and explosive outgassing behavior. The recurrence interval between explosive events can inform on the requisite time for gouge densification in the conduit.

6. Summary

Lava spines produced during the effusive eruption of crystal-rich rhyodacitic magmas often reach the surface enveloped in layers of texturally diverse volcanic fault gouge. The gouge-derived materials extruded during the 2004–2008 eruption at MSH range from unconsolidated powders to low-porosity, low-permeability fault rocks. We investigated the process responsible for the lithification of gouge using observational data collected during the eruption to reconstruct the ascent paths and thermal histories of the extruded lava spines. Using the time–temperature–pressure information given by these reconstructions, and the association of the most competent gouge materials with the spines erupted at the slowest ascent rates, we suggest a new mechanism for the densification and lithification of crystalline volcanic materials at spine-producing volcanoes, including Soufrière Hills, Mount Unzen, Mount Pelée and MSH: the competence of the gouge changes as a result of solid-state sintering, which has a rate dictated by the time–temperature–pressure conditions the gouge experiences in the conduit. When subjected to high pressures and temperatures, small particles coalesce as a result of sintering, and progressively bind larger particles within a densifying matrix. If the material remains at depth for an extended period of time, the gouge will be extensively lithified, and will reach the surface as highly competent material. Increasing gouge competence is accompanied by a reduction in permeability, suggesting lithification of the fault zone decreases outgassing efficiency. Additionally, given the correlation between the physical properties of gouge and its ascent rate, analysis of fault zone rocks mantling lava spines can be used to infer magma ascent rates.

Acknowledgements

We are grateful to the USGS Cascade Volcano Observatory, especially John Pallister, Carl Thornber, David Sherrod, Cynthia Gardner, and Roger Denlinger, for support for our field campaign and for scientific discussion. We thank Peter Frenzen for permitting and for guidance in accessing the Mount St. Helens crater. Alex Kushnir and Stephan Kolzenburg are acknowledged for their help in the field and laboratory. We thank Fabian Wadsworth for providing us with the code for the permeability model from Wadsworth et al. (2016). J.K. Russell acknowledges funding from the NSERC Discovery Grants and Discovery Accelerator Supplements programs (15841). M.J. Heap acknowledges funding from an Initiative d'Excellence (IDEX) "Attractivité" grant (VOLPERM), funded by the University of Strasbourg. The constructive comments of Michael Rowe and one anonymous reviewer helped us improve the quality of this manuscript.

Appendix A. Supplementary material

Supplementary material related to this article can be found online at https://doi.org/10.1016/j.epsl.2017.11.010.

References

Bernstein, M., Pavez, A., Varley, N., Whelley, P., Clader, E.S., 2013. Rhyolite lava dome growth styles at Chaiten Volcano, Chile (2008–2009): interpretation of thermal imagery. Andean Geol. 40, 295–309.

Blundy, J., Cashman, K.V., Berlo, K., 2008. Evolving magma storage conditions beneath Mount St. Helens inferred from chemical variations in melt inclusions from the 1980–1986 and current (2004–2006) eruptions. In: Sherrod, D.R., Scott, W.E., Stauffer, P.H. (Eds.), A Volcano Rekindled: The Renewed Eruption of Mount St. Helens, 2004–2006. In: U.S. Geological Survey Professional Papers, vol. 1750, pp. 755–790.

Bull, K.F., Anderson, S.W., Diefenbach, A.K., Wessels, R.L., Henton, S.M., 2013. Emplacement of the final lava dome of the 2009 eruption of Redoubt Volcano, Alaska. J. Volcanol. Geotherm. Res. 259, 334–348.

Cashman, K.V., Thornber, C.R., Pallister, J.S., 2008. From dome to dust: shallow crystallization and fragmentation of conduit magma during the 2004–2006 dome extrusion of Mount St. Helens, Washington. In: Sherrod, D.R., Scott, W.E., Stauffer, P.H. (Eds.), A Volcano Rekindled: The Renewed Eruption of Mount St. Helens, 2004–2006. In: U.S. Geological Survey Professional Papers, vol. 1750, pp. 387–413.

Cordonnier, B., Hess, K.-U., Lavallée, Y., Dingwell, D.B., 2009. Rheological properties of dome lavas: case study for unzen volcano. Earth Planet. Sci. Lett. 279, 263–272.

Diefenbach, A.K., Crider, J.G., Schilling, S.P., Dzurisin, D., 2012. Rapid, low-cost photogrammetry to monitor volcanic eruptions: an example from Mount St. Helens, Washington, USA. Bull. Volcanol. 74, 579–587.

Fink, J.H., Griffiths, R.W., 1998. Morphology, eruption rates, and rheology of lava domes: insights from laboratory models. J. Geophys. Res., Solid Earth 103, 527–545.

Gaunt, H.E., Sammonds, P.R., Meredith, P.G., Smith, R., Pallister, J.S., 2014. Pathways for degassing during the lava dome eruption of Mount St. Helens 2004–2008. Geology 42, 947–950.

Gerlach, T.M., McGee, K.A., Doukas, M.P., 2008. Emission rates of CO_2, SO_2, and H_2S scrubbing, and preeruption excess volatiles at Mount St. Helens. In: Sherrod, D.R., Scott, W.E., Stauffer, P.H. (Eds.), A Volcano Rekindled: The Renewed Eruption of Mount St. Helens, 2004–2006. In: U.S. Geological Survey Professional Papers, vol. 1750, pp. 543–571.

Goto, A., 1999. A new model for volcanic earthquake at Unzen Volcano: melt rupture model. Geophys. Res. Lett. 26, 2541–2544.

Heap, M.J., Kolzenburg, S., Russell, J.K., Campbell, M.E., Welles, J., Farquharson, J.I., Ryan, A.G., 2014. Conditions and timescales for welding block-and-ash flow deposits. J. Volcanol. Geotherm. Res. 289, 202–209.

Heap, M.J., Russell, J.K., Kennedy, L.A., 2016. Mechanical behavior of dacite from Mount St. Helens (USA): a link between porosity and lava dome extrusion mechanism (dome or spine)? J. Volcanol. Geotherm. Res. 328, 159–177.

Holland, A.S.P., Watson, I.M., Phillips, J.C., Caricchi, L., Dalton, M.P., 2011. Degassing processes during lava dome growth: insights from Santiaguito lava dome, Guatemala. J. Volcanol. Geotherm. Res. 202, 153–166.

Hornby, A.J., Kendrick, J.E., Lamb, O.D., Hirose, T., De Angelis, S., von Aulock, F.W., Umakoshi, K., Miwa, T., De Angelis, S.H., Wadsworth, F.B., Hess, K.-U., Dingwell, D.B., Lavallée, Y., 2015. Spine growth and seismogenic faulting at Mt. Unzen, Japan. J. Geophys. Res., Solid Earth 120, 4034–4054.

Iverson, R.M., Dzurisin, D., Gardner, C.A., Gerlach, T.M., LaHusen, R.G., Lisowiski, M., Major, J.J., Malone, S.D., Messerich, J.A., Moran, S.C., Pallister, J.S., Qamar, A.I., Schilling, S.P., Vallence, J.W., 2006. Dynamics of seismogenic volcanic extrusion at Mount St. Helens in 2004–05. Nature 444, 439–443.

Jaluria, Y., Torrance, K.E., 1986. Computational Heat Transfer. Hemisphere Publishing Corp., Washington, DC. 378 pp.

Kendrick, J.E., Lavallée, Y., Ferk, A., Perugini, D., Leonhardt, R., Dingwell, D.B., 2012. Extreme frictional processes in the volcanic conduit of Mount St. Helens (USA) during the 2004–2008 eruption. J. Struct. Geol. 38, 61–76.

Kendrick, J.E., Lavallée, Y., Hirose, T., Di Toro, G., De Angelis, S., Dingwell, D.B., 2014. Volcanic drumbeat seismicity caused by stick-slip motion and magmatic frictional melting. Nat. Geosci. 7, 438–442.

Kennedy, L.A., Russell, J.K., 2012. Cataclastic production of volcanic ash at Mount Saint Helens. Phys. Chem. Earth 45, 40–49.

Kennedy, L.A., Russell, J.K., Nelles, E., 2009. Origins of Mount St. Helens cataclasites: experimental insights. Am. Mineral. 94, 995–1004.

Kushnir, A.R.L., Kennedy, L.A., Misra, S., Benson, P., White, J.C., 2015. The mechanical and microstructural behavior of calcite–dolomite composites: an experimental investigation. J. Struct. Geol. 70, 200–216.

Lamb, O.D., De Angelis, S., Umakoshi, K., Hornby, A.J., Kendrick, J.E., Lavallée, Y., 2015. Repetitive fracturing during spine extrusion at Unzen volcano, Japan. Solid Earth 6, 1277–1293.

Lavallée, Y., Benson, P.M., Heap, M.J., Hess, K.-U., Flaws, A., Schillinger, B., Meredith, P.G., Dingwell, D.B., 2013. Reconstructing magma failure and the degassing network of dome-building eruptions. Geology 41, 515–518.

Lavallée, Y., Hess, K.-U., Cordonnier, B., Dingwell, D.B., 2007. A non-Newtonian rheological law for highly-crystalline dome lavas. Geology 35, 843–846.

Lavallée, Y., Mitchell, T.M., Heap, M.J., Vasseur, J., Hess, K.-U., Hirose, T., Dingwell, D.B., 2012. Experimental generation of volcanic pseudotachylytes: constraining rheology. J. Struct. Geol. 38, 222–233.

Mastin, L.G., Lisowski, M., Roeloffs, E., Beeler, N., 2009. Improved constrains on the estimated size and volatile content of the Mount St. Helens magma system from the 2004–2008 history of dome growth and deformation. Geophys. Res. Lett. 26, L20304.

Minakami, T., Ishikawa, T., Yagi, K., 1951. The 1944 eruption of Volcano Usu in Hokkaido, Japan. Bull. Volcanol. 11, 45–157.

Moran, S.C., Malone, S.D., Qamar, A.I., Thelen, W.A., Wright, A.K., Caplan-Auerbach, J., 2008a. Seismicity associated with renewed dome building at Mount St. Helens. In: Sherrod, D.R., Scott, W.E., Stauffer, P.H. (Eds.), A Volcano Rekindled: The Renewed Eruption of Mount St. Helens, 2004–2006. In: U.S. Geological Survey Professional Papers, vol. 1750, pp. 27–60.

Moran, S.C., McChesney, P.J., Lockhart, A.B., 2008b. Seismicity and infrasound associated with explosions at Mount St. Helens, 2004–2005. In: Sherrod, D.R., Scott, W.E., Stauffer, P.H. (Eds.), A Volcano Rekindled: The Renewed Eruption of Mount St. Helens, 2004–2005. In: U.S. Geological Survey Professional Papers, vol. 1750, pp. 111–127.

Nakada, S., Motomura, Y., 1999. Petrology of the 1991–1995 eruption at Unzen: effusion pulsation and groundmass crystallization. J. Volcanol. Geotherm. Res. 89, 173–196.

Nakada, S., Shimizu, H., Ohta, K., 1999. Overview of the 1990–1995 eruption at Unzen Volcano. J. Volcanol. Geotherm. Res. 89, 1–22.

Neuberg, J.W., Tuffen, H., Collier, L., Green, D., Powell, T., Dingwell, D.B., 2006. The trigger mechanism for low-frequency earthquakes at Montserrat. J. Volcanol. Geotherm. Res. 153, 37–50.

Okumura, S., Kushnir, A.R.L., Martel, C., Champallier, R., Thibault, Q., Takeuchi, S., 2016. Rheology of crystal-bearing natural magmas: torsional deformation experiments at 800 °C and 100 MPa. J. Volcanol. Geotherm. Res. 328, 237–246.

Pallister, J.S., Cashman, K.V., Hagstrum, J.T., Beeler, N.M., Moran, S.C., Denlinger, R.P., 2013. Faulting within the Mount St. Helens conduit and implications for volcanic earthquakes. Geol. Soc. Am. Bull. 125, 359–376.

Pallister, J.S., Thornber, C.R., Cashman, K.V., Clynne, M.A., Lowers, H.A., Mandeville, C.W., Brownfield, I.K., Meeker, G.P., 2008. Petrology of the 2004–2006 Mount St. Helens lava dome – implication for magmatic plumbing and eruption triggering. In: Sherrod, D.R., Scott, W.E., Stauffer, P.H. (Eds.), A Volcano Rekindled: The Renewed Eruption of Mount St. Helens, 2004–2006. In: U.S. Geological Survey Professional Papers, vol. 1750, pp. 647–702.

Poland, M.P., Dzurisin, D., LaHusen, R.G., Major, J.J., Lapcewich, D., Endo, E.T., Gooding, D.J., Schilling, S.P., Janda, C.G., 2008. Remote camera observations of lava dome growth at Mount St. Helens, Washington, October 2004 to February 2006. In: Sherrod, D.R., Scott, W.E., Stauffer, P.H. (Eds.), A Volcano Rekindled: The Renewed Eruption of Mount St. Helens, 2004–2006. In: U.S. Geological Survey Professional Papers, vol. 1750, pp. 225–236.

Quane, S.L., Russell, J.K., Friedlander, E.A., 2009. Time scales of compaction in volcanic systems. Geology 37, 471–474.

Rahaman, M.N., 2003. Ceramic Processing and Sintering. Marcel Dekker Inc., New York, NY. 875 pp.

Ramqvist, L., 1966. Theories of hot pressing. Powder Metall. 9, 1–25.

Rowe, M.C., Thornber, C.R., Kent, A.J.R., 2008. Identification and evolution of the juvenile component in 2004–2005 Mount St. Helens ash. In: Sherrod, D.R., Scott, W.E., Stauffer, P.H. (Eds.), A Volcano Rekindled: The Renewed Eruption of Mount St. Helens, 2004–2006. In: U.S. Geological Survey Professional Papers, vol. 1750, pp. 629–646.

Russell, J.K., 1988. Aspects of heat transfer in magmas. In: Nisbet, E.G., Fowler, C.M.R. (Eds.), Heat, Metamorphism and Tectonics. In: Short Course Handbook, vol. 14. Mineralogical Association of Canada, pp. 115–155.

Ryan, G.A., Loughlin, S.C., James, M.R., Jones, L.D., Clader, E.S., Christopher, T., Strutt, M.H., Wadge, G., 2010. Growth of the lava dome and extrusion rates at Soufriere Hills Volcano, Montserrat, West Indies: 2005–2008. Geophys. Res. Lett. 37, L00E08.

Rybacki, E., Paterson, M.S., Wirth, R., Dresen, G., 2003. Rheology of calcite–quartz aggregates deformed to large strain in torsion. J. Geophys. Res., Solid Earth 108 (B2), 2089.

Schilling, S.P., Thompson, R.A., Messerich, J.A., Iwatsubo, E.Y., 2008. Use of digital aerophotogrammetry to determine rates of lava dome growth, Mount St. Helens, Washington. In: Sherrod, D.R., Scott, W.E., Stauffer, P.H. (Eds.), A Volcano Rekindled: The Renewed Eruption of Mount St. Helens, 2004–2006. In: U.S. Geological Survey Professional Papers, vol. 1750, pp. 145–167.

Scott, W.E., Sherrod, D.R., Gardner, C.A., 2008. Overview of the 2004 to 2006, and continuing, eruption of Mount St. Helens, Washington. In: Sherrod, D.R., Scott, W.E., Stauffer, P.H. (Eds.), A Volcano Rekindled: The Renewed Eruption of Mount St. Helens, 2004–2006. In: U.S. Geological Survey Professional Papers, vol. 1750, pp. 3–22.

Smith, R., Sammonds, P.R., Tuffen, H., Meredith, P.G., 2011. Evolution of the mechanics of the 2004–2008 Mt. St. Helens lava dome with time and temperature. Earth Planet. Sci. Lett. 307, 191–200.

Sparks, R.S.J., Murphy, M.D., Lejeune, A.M., Watts, R.B., Barclay, J., Young, S.R., 2000. Control on the emplacement of the andesite lava dome of the Soufriere Hills volcano, Montserrat by degassing-induced crystallization. Terra Nova 12, 14–20.

Thiele, S.T., Varley, N., James, M.R., 2017. Thermal photogrammetric imaging: a new technique for monitoring dome eruptions. J. Volcanol. Geotherm. Res. 337, 140–145.

Thornber, C.R., Pallister, J.S., Rowe, M.C., McConnell, S., Herriott, T.M., Eckberg, A., Stokes, W.C., Johnson Cornelius, D., Conrey, R.M., Hannah, T., Taggart, J.E., Adams, M., Lamothe, P.J., Budahn, J.R., Knaack, C.M., 2008. Catalog of Mount St. Helens 2004–2007 Dome Samples with Major and Trace-Element Chemistry. U.S. Geological Survey Open File Report 2008-1130.

Umakoshi, K., Takamura, N., Shinzato, N., Uchida, K., Matsuwo, N., Shimizu, H., 2008. Seismicity associated with the 1991–1995 dome growth at Unzen Volcano, Japan. J. Volcanol. Geotherm. Res. 175, 91–99.

Vallance, J.W., Schneider, D.J., Schilling, S.P., 2008. Growth of the 2004–2006 lava-dome complex at Mount St. Helens, Washington. In: Sherrod, D.R., Scott, W.E., Stauffer, P.H. (Eds.), A Volcano Rekindled: The Renewed Eruption of Mount St. Helens, 2004–2006. In: U.S. Geological Survey Professional Papers, vol. 1750, pp. 169–208.

Vasseur, J., Wadsworth, F.B., Lavallée, Y., Hess, K.-U., Dingwell, D.B., 2013. Volcanic sintering: timescales of viscous densification and strength recovery. Geophys. Res. Lett. 40, 5658–5664.

Wadsworth, F.B., Vasseur, J., Llewellin, E.W., Dingwell, D.B., 2017. Sintering of polydisperse viscous droplets. Phys. Rev. E 95, 033114.

Wadsworth, F.B., Vasseur, J., Scheu, B., Kendrick, J.E., Lavallée, Y., Dingwell, D.B., 2016. Universal scaling of fluid permeability during volcanic welding and sediment diagenesis. Geology 44, 219–222.

Watts, R.B., Herd, R.A., Sparks, R.S.J., Young, S.R., 2002. Growth patterns and emplacement of the andesitic lava dome at Soufrière Hills volcano. In: Druitt, T.H., Kokelaar, B.R. (Eds.), The Eruption of Soufriere Hills Volcano, Montserrat from 1995–1999. In: Mem. Geol. Soc. Lond., vol. 21, pp. 115–152.

White, J., 1965. Sintering: an assessment. Proc. Br. Ceram. Soc. 3, 155–176.